

COLLISIONAL DISRUPTION OF GRAVITATIONAL AGGREGATES IN THE TIDAL ENVIRONMENT

RYUKI HYODO¹ AND KEIJI OHTSUKI^{1,2}

¹ Department of Earth and Planetary Sciences, Kobe University, Kobe 657-8501, Japan

² Laboratory for Atmospheric and Space Physics, University of Colorado, Boulder, CO 80303, USA

Received 2013 September 13; accepted 2014 April 2; published 2014 May 2

ABSTRACT

The degree of disruption in collisions in free space is determined by specific impact energy, and the mass fraction of the largest remnant is a monotonically decreasing function of impact energy. However, it has not been shown whether such a relationship is applicable to collisions under the influence of a planet’s tidal force, which is important in ring dynamics and satellite accretion. Here we examine the collisional disruption of gravitational aggregates in the tidal environment by using local N -body simulations. We find that outcomes of such a collision largely depend on the impact velocity, the direction of impact, and the radial distance from the planet. In the case of a strong tidal field corresponding to Saturn’s F ring, collisions in the azimuthal direction are much more destructive than those in the radial direction. Numerical results of collisions sensitively depend on the impact velocity, and a complete disruption of aggregates can occur even in impacts with velocity much lower than their escape velocity. In such low-velocity collisions, the deformation of colliding aggregates plays an essential role in determining collision outcomes, because the physical size of the aggregate is comparable to its Hill radius. On the other hand, the dependence of collision outcomes on impact velocity becomes similar to the case in free space when the distance from the planet is sufficiently large. Our results are consistent with *Cassini* observations of the F ring, which suggest ongoing creation and disruption of aggregates within the ring.

Key words: planets and satellites: dynamical evolution and stability – planets and satellites: formation – planets and satellites: rings

Online-only material: animations, color figures

1. INTRODUCTION

In dynamical evolution of ring–satellite systems of giant planets, collisions under the influence of the planet’s tidal force play an essential role. At radial locations sufficiently interior to the Roche limit, the tidal force prevents colliding particles from becoming gravitationally bound aggregates. However, with increasing distance from the central planet, small particles can become gravitationally bound to larger particles (Weidenschilling et al. 1984; Ohtsuki 1993; Canup & Esposito 1995; Karjalainen & Salo 2004; Karjalainen 2007; Tiscareno et al. 2013; Ohtsuki et al. 2013). Observations of small satellites near the outer edge of Saturn’s A ring by the *Cassini* spacecraft suggest such a gravitational accretion of ring particles in the Roche zone (Porco et al. 2007). The effect of the tidal force becomes negligible far outside the Roche limit, and particles with arbitrary mass ratios are able to form gravitational aggregates. On the other hand, collisions between particles or aggregates in the tidal environment lead not only to accretion but also to disruption. For example, transient brightening events in Saturn’s F ring were reported on the basis of a detailed analysis of *Voyager* images (Showalter 1998), and a collision between embedded bodies has been proposed as the cause of these events (Barbara & Esposito 2002). More recently, small protrusions from the core of the F ring, called “mini-jets,” have been observed by *Cassini*, and they are regarded as showing low-velocity collisions within the ring (Attree et al. 2012). Disruptive processes of planetary bodies have been extensively studied in the contexts of planetary accretion or asteroid dynamics (e.g., Stewart & Leinhardt 2009; Leinhardt & Stewart 2012 and references therein). However, since the effect of the tidal force is not taken into account in these works, we cannot directly apply results of these studies to ring–satellite systems. In the present

work, we will investigate criteria for collisional disruption in the Roche zone.

In theoretical studies of ring dynamics, it is often assumed that ring particles are inelastic hard spheres. However, it is likely that they are weakly bound gravitational aggregates consisting of smaller particles. At radial locations sufficiently inside the Roche limit, gravitational accretion of particles does not take place (Ohtsuki et al. 2013). When an aggregate is placed just inside the Roche limit in a synchronous state, tidal disruption occurs and particles are released through the vicinity of the lowest potential points, i.e., the Lagrange points (Leinhardt et al. 2012). On the other hand, at radial locations far outside the Roche limit, particles can form gravitational aggregates (Karjalainen & Salo 2004). At the radial location of the F ring, which is barely outside the Roche limit, even though gravitational aggregates are formed, the size of a stable aggregate itself and that of its Hill sphere are comparable. As a result, even a slight deformation from its stable shape due to a collision with other particles or aggregates would lead some particles to become gravitationally unbound, which would then result in total disruption of the aggregate. Therefore, it is likely that even stable aggregates are vulnerable to collisional disruption in the Roche zone.

Aggregate collisions in free space have been studied in detail in the contexts of asteroid or planetesimal dynamics (Leinhardt et al. 2000; Leinhardt & Richardson 2002; Takeda & Ohtsuki 2007, 2009; Stewart & Leinhardt 2009; Leinhardt & Stewart 2012). On the other hand, Walsh & Richardson (2003) first examined collisions between gravitational aggregates in the tidal environment. They conducted N -body simulations of collisions between gravitational aggregates in a strong tidal field corresponding to Saturn’s F ring. Their results show that collision outcomes in such a case strongly depend on the impact

speed and the coefficient of restitution. However, they focused on the case of the F ring and did not study the dependence of collision outcomes on radial distance from the planet. Moreover, they assumed that the initial shape of colliding aggregates was spherical, neglecting deformation due to the tidal force. In fact, Karjalainen (2007) performed similar impact simulations in the tidal environment, taking into account the elongated shape of aggregates and found that more elongated aggregates are more prone to be destroyed. He performed local N -body simulations of collisions between gravitational aggregates in the Roche zone for a wide range of parameters and showed that the accretion probability increases with increasing distance from the planet. In the case of collisions at the radial location of the F ring, he also examined the dependence of the outcome on the impactor–target mass ratio and confirmed that colliding aggregates that greatly differ in mass can more easily accrete (Ohtsuki 1993; Canup & Esposito 1995) and the accretion efficiency is higher than the results obtained by three-body calculations that assume ring particles are hard spheres (Ohtsuki 1993). However, calculations reported in Karjalainen (2007) were limited to the case with initially coplanar circular orbits. Actual aggregates in ring–satellite systems are expected to have finite orbital eccentricities and inclinations due to collisions and/or gravitational interactions with other ring particles/aggregates or satellites, especially in the F ring perturbed by the shepherding satellites. When aggregates have eccentricities or inclinations, their impact velocities as well as impact angles are expected to differ from those of initially coplanar circular orbits; thus, collision outcomes would also be different.

Recent *Cassini* images of the F ring imply that perturbations by the shepherding satellites likely assist the ring particles' gravitational instability and formation of gravitational clumps, while these aggregates can also be disrupted by collisions, as mentioned above (Beurle et al. 2010; Attree et al. 2012). In order to understand the criteria and efficiency of accretion and disruption of these gravitational aggregates, we need to investigate the process of collisional disruption in the tidal field in detail. Aggregate collisions in the Roche zone would also be a key to understand the process of satellite formation from circumplanetary particle disks (Charnoz et al. 2010; Crida & Charnoz 2012).

In the present work, we investigate the process of collisional disruption of gravitational aggregates in the tidal field using local N -body simulations. In particular, we focus on the Saturnian system and investigate the dependence of collision outcomes on the impact velocity, the direction of impact, and the radial distance from the planet, although our results can also be applied to other ring–satellite systems. In Section 2, the conditions of gravitational accretion and impact velocity in the tidal field are briefly described. In Section 3, we describe our numerical methods. Section 4 presents our numerical results of impact simulations. In Section 5, we discuss the criteria for catastrophic disruption, and our conclusions are summarized in Section 6.

2. ACCRETION CRITERIA AND IMPACT VELOCITY IN THE ROCHE ZONE

2.1. Accretion Criteria in the Roche Zone

First, we briefly describe accretion criteria in the Roche zone, which is useful in understanding the disruption criteria we discuss in later sections. Suppose that a synchronously rotating fluid satellite with no material strength is moving in a circular orbit around a central planet under its tidal force. The critical

radial distance inside of which the satellite is tidally disrupted is given by (Roche 1847; Chandrasekhar 1969)

$$a_R = 2.456 \left(\frac{\rho_c}{\rho} \right)^{1/3} R_c, \quad (1)$$

where ρ , ρ_c and R_c are the mean densities of the satellite and the planet and the radius of the planet, respectively. This critical distance is called the classical Roche limit. On the other hand, in the case of radially aligned, equal-sized spherical solid satellites touching each other, the critical distance for their gravitational accretion is given by (Weidenschilling et al. 1984)

$$a = 2.29 \left(\frac{\rho_c}{\rho} \right)^{1/3} R_c. \quad (2)$$

Similarly, the critical distance for a small particle to be gravitationally bound to a much larger, radially aligned satellite is given by (Weidenschilling et al. 1984)

$$a = 1.44 \left(\frac{\rho_c}{\rho} \right)^{1/3} R_c. \quad (3)$$

We can derive the accretion criteria in a more general form by using the kinetic energy of colliding particles rather than their mutual gravitational force (Ohtsuki 1993; Ohtsuki et al. 2013; see also Schmidt et al. 2009).

The ratio of the sum of the radii of colliding particles to their mutual Hill radius is an important physical quantity related to the accretion criteria in the Roche zone. Here the Hill radius R_H for particles orbiting at a radial distance a from the central planet is given as

$$R_H \equiv \left(\frac{m_1 + m_2}{3M_c} \right)^{1/3} a, \quad (4)$$

and the ratio is given by

$$\tilde{r}_p = (R_1 + R_2)/R_H, \quad (5)$$

where M_c is the mass of the central planet, and R_1, R_2, m_1 , and m_2 are the radii and masses of the colliding particles, respectively. Note that the criteria (2) and (3) correspond to $\tilde{r}_p = 1$ with $R_1 = R_2$ and with $R_1 \gg R_2$, respectively. The above accretion condition can also be expressed in terms of the mean density of accreting particles (Porco et al. 2007; Tiscareno et al. 2013). That is, gravitational accretion is possible when $\rho > \rho_{\text{crit}}$ with

$$\rho_{\text{crit}} = \frac{3M_c}{\gamma a^3}, \quad (6)$$

where γ is a dimensionless shape parameter so that γR_{sat}^3 is the volume of the satellite, with R_{sat} being the long semi-axis of the satellite ($\gamma = 4\pi/3$ for a spherical satellite with radius R_{sat}). The condition $\rho > \rho_{\text{crit}}$ is equivalent to $\tilde{r}_p < 1$. \tilde{r}_p can also be expressed by using the semimajor axis, density, and the mass ratio of the colliding particles as

$$\tilde{r}_p = \frac{R_c}{a} \left(\frac{\rho}{3\rho_c} \right)^{-1/3} \frac{1 + \mu^{1/3}}{(1 + \mu)^{1/3}}, \quad (7)$$

where $\mu = m_1/m_2$. For example, in the case of the Saturnian system with particle density 0.9 g cm^{-3} , we have $a_R \simeq 135,000 \text{ km}$, and when $\mu = 1$, Equation (7) can be rewritten as

$$\tilde{r}_p \simeq 0.9 \times \left(\frac{\rho}{0.9 \text{ g cm}^{-3}} \right)^{-1/3} \left(\frac{a}{140,000 \text{ km}} \right)^{-1}. \quad (8)$$

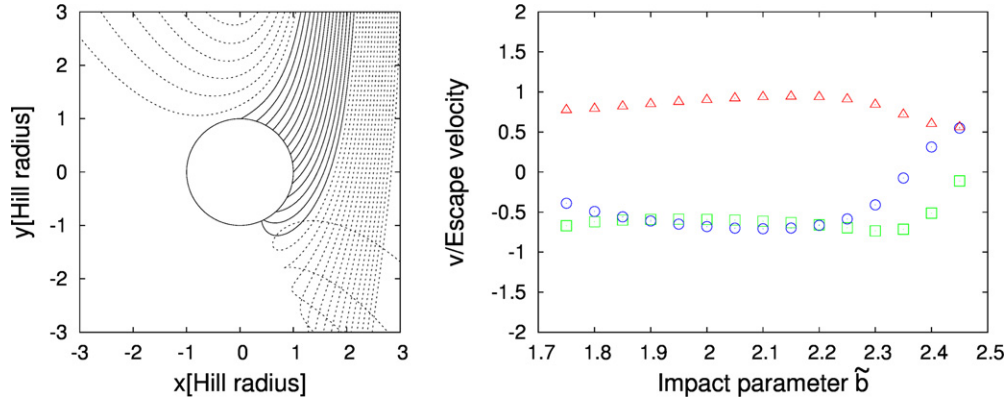


Figure 1. Numerical results of three-body orbital calculations for particles initially on circular and coplanar orbits ($e = i = 0$, $\tilde{r}_p = 1$). The left panel shows particle orbits for various values of the nondimensional impact parameter \tilde{b} . The solid circle represents the physical size of the colliding particles. The solid lines represent trajectories that lead to collision, and the dotted lines represent non-collision trajectories. The right panel shows the magnitude of impact velocity (red triangles) as well as its radial (green squares) and azimuthal (blue circles) components, respectively, as a function of impact parameter.

(A color version of this figure is available in the online journal.)

Assuming that particles are inelastic hard spheres, Ohtsuki (1993) performed three-body calculations for the accretion probability of colliding particles in the Roche zone and found that $\tilde{r}_p \lesssim 0.7$ is required for significant accretion in the case of particles with low random velocities. This is because the physical size of the particles overflow their mutual Hill sphere when $\tilde{r}_p > 2/3$ and thus accretion becomes difficult. On the other hand, in the case of collision between gravitational aggregates consisting of small particles, accretion is facilitated because of the adjustment of their shape at collision (Karjalainen 2007).

2.2. Impact Velocity

Whether colliding particles can gravitationally accrete or not also depends on their impact velocity. Three-body orbital calculations show that the accretion probability drops rapidly when the impact velocity becomes comparable to or higher than the escape velocity, even if $\tilde{r}_p < 2/3$ (Ohtsuki 1993; Ohtsuki et al. 2013). Outcomes of collisional disruption in the tidal environment should also depend on impact velocity. Magnitude and direction of impact velocity vary with orbital elements of colliding bodies. Here, as examples, we examine radial and azimuthal components of impact velocity for two cases (i.e., initially circular and elliptic orbits), using three-body orbital integration.

We consider the motion of two particles i and j in a rotating Cartesian coordinate system (x, y, z) with the origin moving on a circular orbit at the distance a_0 from the central planet with the Keplerian angular velocity Ω , where the x -axis is pointing radially outward, the y -axis is pointing toward the orbital motion, and the z -axis is perpendicular to the x - y plane. Suppose that the mass and position vector of particle i are given by m_i and $\mathbf{r}_i = (x_i, y_i, z_i)$, respectively. In this case, linearized equations of motion for particle i are described as

$$\begin{aligned} \ddot{x}_i &= 2\Omega\dot{y}_i + 3\Omega^2 x_i + \frac{Gm_j(x_j - x_i)}{r_{ij}^3} \\ \ddot{y}_i &= -2\Omega\dot{x}_i + \frac{Gm_j(y_j - y_i)}{r_{ij}^3} \\ \ddot{z}_i &= -\Omega^2 z_i + \frac{Gm_j(z_j - z_i)}{r_{ij}^3}, \end{aligned} \quad (9)$$

where $\mathbf{r}_{ij} \equiv |\mathbf{r}_i - \mathbf{r}_j|$. The equations for the relative motion can be written in a form similar to Equation (9) (Nakazawa et al. 1989; Ohtsuki 2012), which we solve to obtain relative velocities at impact.

Figure 1 shows outcomes of three-body orbital integration for particles initially on coplanar circular orbits (i.e., $e = i = 0$, where e and i are orbital eccentricity and inclination for the relative motion, respectively). We consider the case where $\tilde{r}_p = 1$. The left panel shows particle trajectories. Solid lines represent trajectories that lead to collision, while non-collision orbits are shown with dotted lines. The solid circle shows the physical size of the colliding particles; the radius of the circle corresponds to the sum of the radii of the colliding particles in units of R_H . The right panel shows the magnitude of impact velocity as well as its radial and azimuthal components as a function of the nondimensional impact parameter $\tilde{b} = (a_i - a_j)/R_H$, where a_i and a_j are the semimajor axes of colliding bodies. We find that in the case of initially circular orbits, the magnitudes of impact velocities are approximately given by the mutual escape velocity, $v_{\text{esc}} = \sqrt{2G(m_i + m_j)/(R_i + R_j)}$. On the other hand, we find that the magnitudes of each velocity component vary significantly. In many cases, the radial and azimuthal components are comparable to each other, but in some cases one component is dominant over the other. Figure 2 shows similar plots for the case of initially elliptic orbits ($\tilde{e} = ea_0/R_H = 5$). Because of the particles' random velocity, impact velocities are higher in the present case than in the case of circular orbits (Figure 2, right panels). Again, we find that the x and y components of the impact velocities largely vary with \tilde{b} and the orbital phase, and in some cases collisions are nearly in the radial ($|v_x| \gg |v_y|$ and $|v_z| = 0$) or azimuthal ($|v_x| \ll |v_y|$ and $|v_z| = 0$) direction. Also, when particles have nonzero inclinations, collisions can be nearly in the vertical direction ($|v_z| \gg |v_x|, |v_y|$). Therefore, diverse combinations of impact velocities and their components can be expected, depending on particles' random velocity, impact parameter, and orbital phase angles.

As we will show in Section 4, in the case of collisions in the tidal environment, collision outcomes sensitively depend not only on the magnitude of impact velocity but also on the direction of impact. In the present work, in order to clarify the basic characteristics of collisional disruption processes of gravitational aggregates in the tidal environment, we will focus

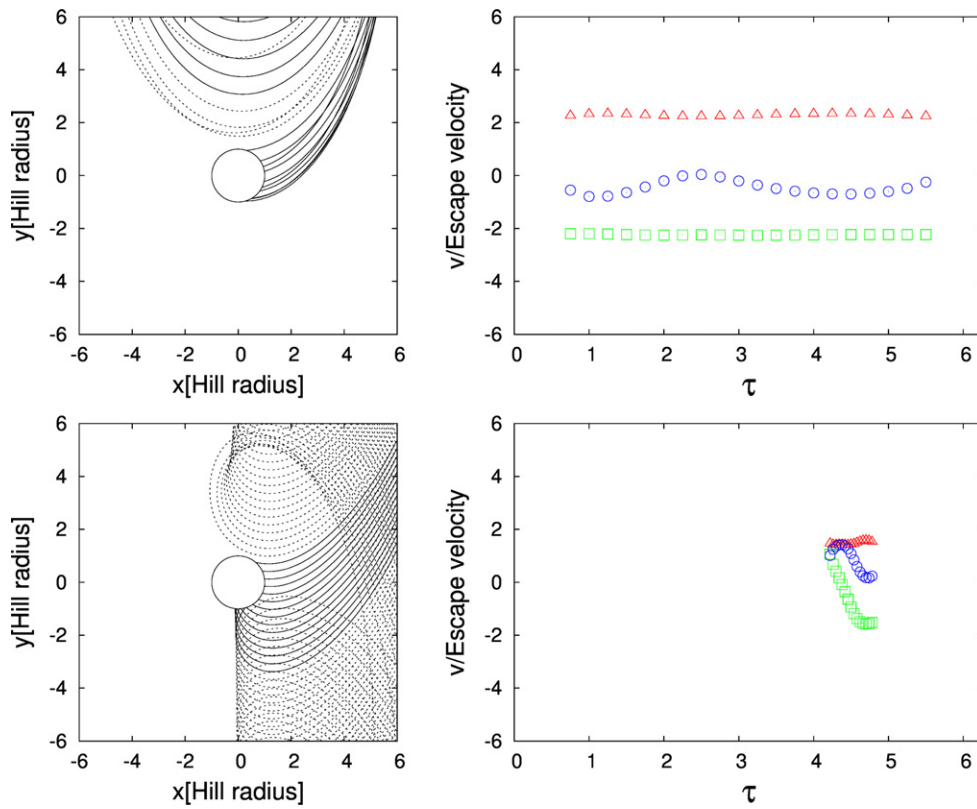


Figure 2. Numerical results of three-body orbital calculations for particles initially on coplanar elliptic ($\tilde{e} = 5$, $\tilde{r}_p = 1$) orbits. The left panels show particle trajectories for $\tilde{b} = 1.15$ (top) and 5.0 (bottom), respectively, with various orbital phases. As in Figure 1, the solid lines represent trajectories that lead to collision, while the dotted lines represent non-collision orbits. The right panels show the magnitude of impact velocity (red triangles) as well as its radial (green squares) and azimuthal (blue circles) components, respectively, as a function of the horizontal phase angle τ .

(A color version of this figure is available in the online journal.)

on radial ($|v_x| \neq 0$, $v_y = v_z = 0$), azimuthal ($v_x = v_z = 0$, $|v_y| \neq 0$), and vertical ($v_x = v_y = 0$, $|v_z| \neq 0$) collisions. We will vary impact velocities as a parameter and examine criteria for disruption.

3. NUMERICAL METHODS

We perform simulations of aggregate collisions using our local N -body simulation code that deals with gravitational interactions and inelastic collisions between particles in the Hill coordinate system. Particle trajectories are integrated by using the second order symplectic leapfrog method (Quinn et al. 2010). When collisions between particles are detected, velocity changes are calculated on the basis of the hard-sphere model. We assume that particles are smooth spheres with a normal coefficient of restitution, ε_n .

We proceed by taking the following three steps. First, 500 identical particles are randomly distributed in a low-density sphere in isolation, where the gravitational potential of the planet is not included, and we let the particles collapse into their center of mass due to their mutual gravity. We assume that particle collisions are highly inelastic ($\varepsilon_n = 0.1$) at this stage so that relative motion of the particles is damped quickly. Second, after a rubble pile is formed, it is placed at the origin of the Hill coordinate system, where the gravitational force of the central planet is now turned on. The motion of the particles in the system is then integrated, and the rubble pile sphere is deformed into an ellipsoid-like shape because of the tidal force of the planet. Then, as the third step, we perform impact simulations using this deformed rubble pile. Two identical aggregates are placed in the

Hill coordinate system, so that initially they are just touching each other, either in the radial, azimuthal, or vertical direction as shown in Figure 3. Then, an initial velocity of the same magnitude but in the opposite direction is given to each of the aggregates, so that the center of mass of the system is fixed at the origin (Figure 3). At the above initial state, the velocity of each aggregate is exactly pointing toward the center of the other. After the start of the simulation, it takes a finite period of time before the aggregates overlap significantly, and in the case of radial or azimuthal collisions, the trajectory of each aggregate slightly curves to the right from its original direction because of the Coriolis force (the terms $2\Omega\dot{y}_i$ and $-2\Omega\dot{x}_i$ on the right-hand side of Equation (9)) during this short period of time. However, we adopt the above initial state and give impact velocity as a parameter, because in this way we can easily examine the dependence of collision outcomes on impact direction with given impact velocities and easily compare our results with those of head-on collisions in free space. In most of our simulations, we assume $\varepsilon_n = 0.25$ in the second and third steps. We examine the dependence on the restitution coefficient in Section 4.3.

A collision between the two aggregates can result in total accretion, complete disruption, or partial disruption with reaccretion of some of constituent particles, depending on parameters. At the end of each simulation, we examine the masses of the largest and the second largest remnant aggregates, in order to investigate the degree of disruption. Note that we continue our numerical calculations until the system achieves a quasi-steady state, where further change in the masses of the largest and the second largest remnant aggregates can be neglected (Figure 4).

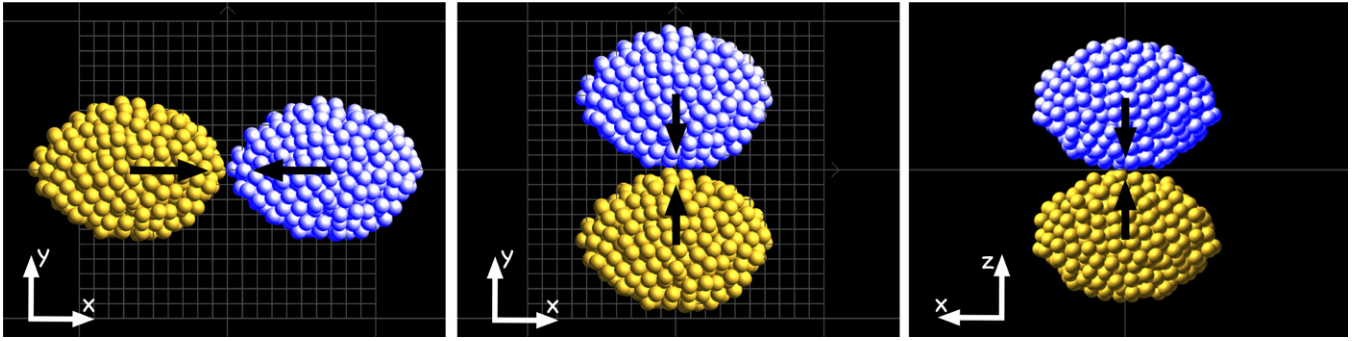


Figure 3. Illustration of the initial condition of our impact simulation. Two aggregates are initially touching each other. The left, middle, and right panels show radial, azimuthal, and vertical collisions, respectively, in the rotating coordinate system. In the left and middle panels, the central planet is to the left, and orbital motion is upward. In the right panel, the central planet is to the right. The black arrows show the directions of initial velocities that we give to the constituent particles of each aggregate.

(A color version of this figure is available in the online journal.)

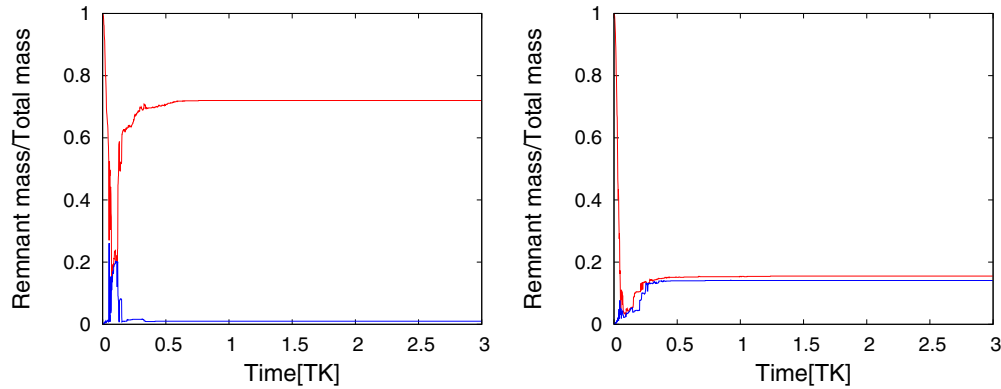


Figure 4. Examples of the time evolution of the mass of the largest (red line) and the second largest (blue line) remnants. The left and right panels show results of radial collisions between ellipsoid-like aggregates at $a = 200,000$ km with $v_{\text{imp}} = 3.19v_{\text{esc}}$ and $v_{\text{imp}} = 3.82v_{\text{esc}}$, respectively (v_{esc} is the escape velocity of a spherical body that has the mass of the initial aggregate with particle density of 0.9 g cm^{-3}). Time is scaled by the orbital period at the radial location of the origin of the system. At the initial state, the two aggregates as a whole is regarded as the largest remnant because the aggregates are touching each other; thus, the mass of the largest remnant equals the total mass. As shown in these plots, collision outcomes achieve quasi-steady states after a certain period of time. All our numerical calculations were continued until the system reaches such a quasi-steady state.

(A color version of this figure is available in the online journal.)

The equilibrium shape of gravitational aggregates depends on the radial distance from the planet, and Karjalainen (2007) showed that outcomes of collisions in the tidal environment depend on the initial shape of aggregates. In order to eliminate the influence of the aggregate shape, Karjalainen (2007) used the same aggregate shape in simulations for various radial locations. Following Karjalainen (2007), we also use the same aggregate that is constructed from 500 identical particles with density 0.9 g cm^{-3} and has a certain aspect ratio in simulations at various radial distances from the planet. The aggregate we use is the one created in the way described above for $a = 140,000$ km from Saturn, and it has the ratios of the semi-principal axis lengths of $Y/X \approx 0.71$ and $Z/Y \approx 0.98$. In this case, the volume density (or filling factor) ≈ 0.73 . For comparison, we also perform simulations with spherical aggregates in the case of weak tidal effect ($a = 200,000$ km; Section 4.2).

As a test of our simulation code, we performed simulations of impacts between aggregates initially on circular orbits as done by Karjalainen (2007), and we confirmed agreement with his results on accretion probability. We also performed simulations of collision in free space and confirmed agreement with previous works (e.g., Leinhardt & Stewart 2012). A detailed comparison with the case of collision in free space will be discussed in Section 5. In the following, we use parameter values such as the radial distance from the planet corresponding

to the Saturnian system. However, numerical results for a radial location corresponding to a certain value of \tilde{r}_p can be applied to other ring systems, as long as a radial location corresponding to the same value of \tilde{r}_p is considered.

4. RESULTS OF IMPACT SIMULATIONS

4.1. Collisional Disruption in the Strong Tidal Environment

First, as an example of the case of a strong tidal field, we present results for aggregate collisions at $140,000$ km from Saturn, roughly corresponding to the location of the F ring. Figure 5 shows the plots of mass fractions of the largest (red squares) and the second largest (blue circles) remnant aggregates at the end of the simulation, as a function of impact velocity. In the bottom horizontal axis, the impact velocity scaled by the escape velocity is shown, while the upper horizontal axis represents the corresponding value of the impact velocity when the radius of the constituent particles is 130 m and their internal density is 0.9 g cm^{-3} . Note that the impact energy exceeds the gravitational binding energy of the aggregates when the impact velocity is larger than the escape velocity. In the case of collision in free space, the mass fraction of the largest remnant is expected to decrease monotonically with increasing impact velocity (Leinhardt & Stewart 2012). In contrast, outcomes of collisions in the strong tidal field show completely different behavior.

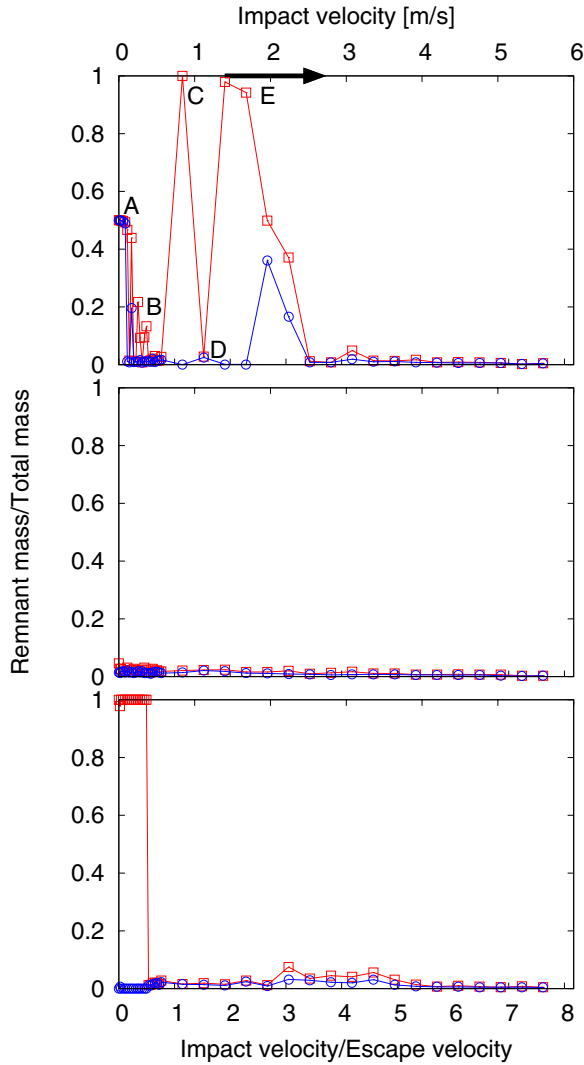


Figure 5. Mass fractions of the largest (red squares) and the second largest (blue circles) aggregates obtained at the end of simulations, as a function of impact velocity in the case of a strong tidal environment corresponding to the location of Saturn’s F ring ($a = 140,000$ km). The top, middle, and bottom panels show the results of radial collision, azimuthal collision, and vertical collision, respectively. The vertical and horizontal axes represent the mass fraction scaled by the total mass of the colliding aggregates, and impact velocity v_{imp} scaled by the escape velocity v_{esc} of a spherical body that has the mass of the initial aggregate with particle density of 0.9 g cm^{-3} , respectively. The upper horizontal axis represents the corresponding value of the impact velocity when the radius of the constituent particles is 130 m and their internal density is 0.9 g cm^{-3} .

(A color version of this figure is available in the online journal.)

The top panel of Figure 5 shows results for radial collisions, where we find complicated dependence of the collision outcome on impact velocity. Figures 6 and 7 show time series of several simulations in this case.³ When the impact velocity is very small, the colliding aggregates become separated because of the

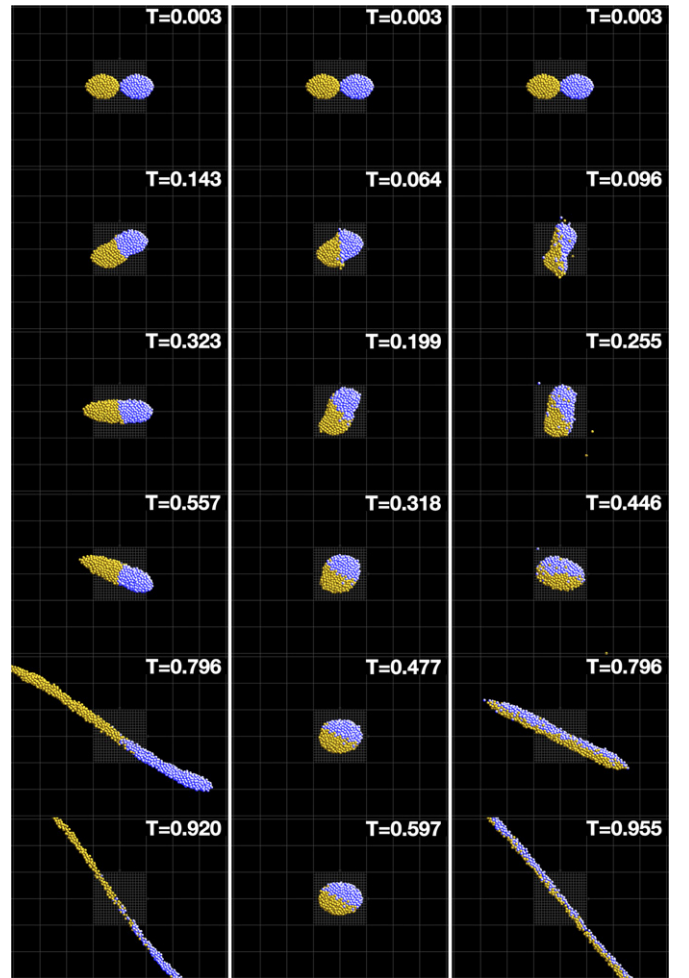


Figure 6. Time series of simulations of collisions between aggregates in the radial direction in the strong tidal environment corresponding to the location of Saturn’s F ring ($a = 140,000$ km). The central planet is to the left, and orbital motion is upward. Three cases of relatively low-velocity impacts are shown. Left: total disruption ($v_{\text{imp}}/v_{\text{esc}} = 0.69$, Region B in Figure 5, left). Middle: total accretion ($v_{\text{imp}}/v_{\text{esc}} = 1.14$, Region C in Figure 5, left). Right: total disruption ($v_{\text{imp}}/v_{\text{esc}} = 1.52$, Region D in Figure 5, left). Numbers in each panel represent the time elapsed since the start of the simulation, in units of the orbital period at the radial location of the origin of the system.

(Animations and a color version of this figure are available in the online journal.)

Coriolis force and the Kepler shear immediately after their first contact. As a result, both aggregates remain nearly intact, the mass of each aggregate being kept close to half of the total mass (Region A in the top panel of Figure 5; this case is not shown in Figure 6 or Figure 7). With a slightly higher impact velocity, the area of the contact surface of the colliding aggregates at the time of impact becomes significant, and the aggregates apparently form a combined object. However, because the mass of the combined object is not sufficiently concentrated around its center of mass, it gradually becomes elongated because of the tidal force. In this case, part of the aggregate overflows its closed zero-potential surface, leading to total disruption with little mixing among constituent particles originated from each aggregate (e.g., the case with $v_{\text{imp}}/v_{\text{esc}} = 0.69$, which is in Region B in Figure 5, top; see also Figure 6, left). This mode of disruption in the low-velocity regime is a direct consequence of the strong tidal effect and never happens in the case of collisions in free space, where lower impact velocities facilitate gravitational accretion. With an additional slight increase in impact velocity, the mass of the combined object formed

³ Movies of the simulations for the cases of Figure 6, middle panel; Figure 6, right panel; and Figure 8, left panel are available as supplemental online material. Note that many of the bottom snapshots in Figures 6–8 do not represent the final state of the simulation. For example, in the case where the final outcome is total disruption (e.g., the left and right panels of Figure 6), after the state shown in the bottom panel, the strung-out line of particles keep shearing out. Then, they experience a secondary gravitational instability on a smaller scale, resulting in destruction of the coherence, as demonstrated in the case of tidal disruption of gravitational aggregates placed in the Roche zone (Leinhardt et al. 2012), and eventually they become completely dispersed (see the movies in supplemental online material).

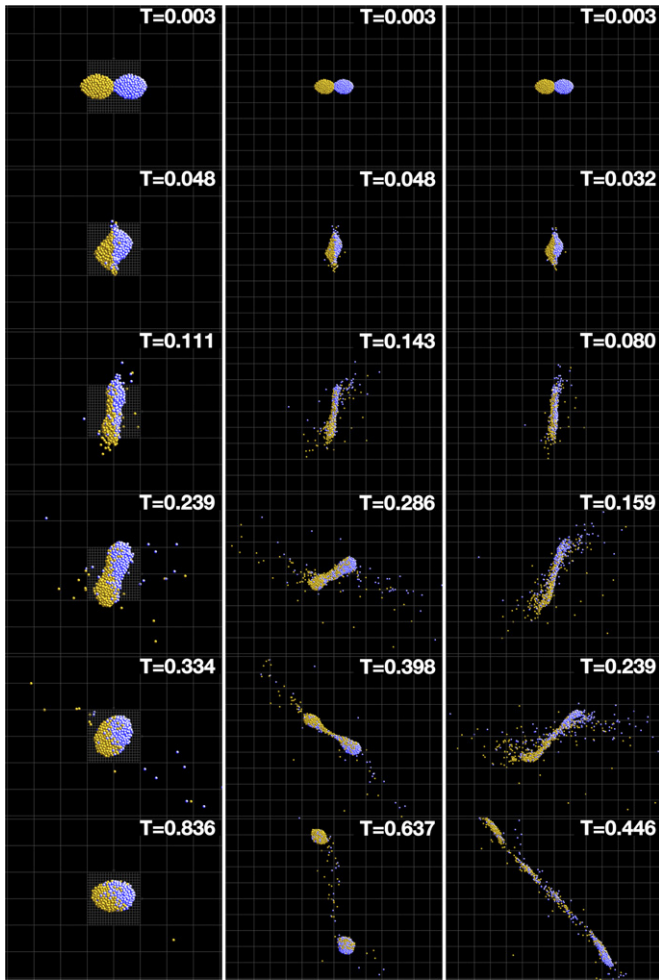


Figure 7. Same as Figure 6, but three cases of relatively high-velocity impacts corresponding to Region E in Figure 5, left, are shown. Left: nearly total accretion ($v_{\text{imp}}/v_{\text{esc}} = 1.90$). Middle: partial accretion ($v_{\text{imp}}/v_{\text{esc}} = 2.67$). Right: total disruption ($v_{\text{imp}}/v_{\text{esc}} = 3.43$).

(A color version of this figure is available in the online journal.)

immediately after collision becomes sufficiently concentrated around its center of mass. This stabilizes the combined object, resulting in total accretion (e.g., the case with $v_{\text{imp}}/v_{\text{esc}} = 1.14$, which is in Region C in Figure 5, top; see also Figure 6, middle). When the impact velocity is slightly increased further from the case of Region C, however, the collision outcome becomes total disruption again (e.g., the case with $v_{\text{imp}}/v_{\text{esc}} = 1.52$, which is in Region D in Figure 5, top; see also Figure 6, right). This is because the combined object rotates counterclockwise around the center of mass after impact because of the Coriolis force. Because of this rotation, the combined aggregate is elongated in the radial direction, resulting in eventual disruption. Note that particles originated from two initial aggregates are well mixed at the time of disruption in this case (Figure 6, right), in contrast to the case in Region B (Figure 6, left). As we have seen above, in these cases of relatively low-velocity impacts under the strong tidal force, the shape of the combined aggregate immediately after the impact plays an important role in determining the final collision outcome.

Figure 7 shows outcomes of impacts in the strong tidal environment with higher impact velocities (corresponding to Region E in Figure 5, top) compared with the cases shown in Figure 6. In the case shown in the left panel of Figure 7, the higher impact velocity somewhat diminishes the rotation effect

mentioned above, resulting in almost total accretion (the case with $v_{\text{imp}}/v_{\text{esc}} = 1.90$). In this case and other cases with still higher impact velocities (i.e., the cases in Region E in Figure 5, top; see also Figure 7, middle and right panels), the mass fraction of the largest remnant is regulated by impact velocity as in the case of collisions in free space, in contrast to the low-velocity regime (Regions A to D) where the aggregate shape after collision regulates the collision outcome. In this high-velocity regime (Region E in Figure 5, top), where the impact energy is large enough, constituent particles in the colliding aggregates can have sufficiently high velocity after impact to escape from the gravity of aggregates, leading to dispersal of the aggregates. As a result, the mass fraction of the largest remnant is a monotonically decreasing function of impact velocity in this regime.

On the other hand, the middle panel of Figure 5 shows results of simulations of azimuthal collisions in the strong tidal environment. In this case, even with zero or very small impact velocity, the accelerated motion in the azimuthal direction due to mutual gravitational attraction between the colliding aggregates causes the Coriolis force in the radial direction. As a result, the combined aggregate becomes elongated in the radial direction quickly. At the radial distance considered here, the value of \tilde{r}_p for a pair of colliding constituent particles is about 0.9 (Equation (8)). In this case, the closed zero-potential surface of the aggregate is almost comparable to its physical size. Therefore, this elongation to the radial direction soon results in total disruption (Figure 8, left). With higher impact velocity, in addition to the effect of tidal elongation of the combined aggregate in the radial direction, some particles have sufficiently high velocity immediately after the impact to escape from the gravity of the combined aggregate, further facilitating disruption (Figure 8, middle and right panels).

The bottom panel of Figure 5 shows results of simulations of vertical collisions at the same radial location. We found that there is a sharp transition between accretion and disruption at $v_{\text{imp}}/v_{\text{esc}} \simeq 0.5$. As described above, at the radial distance considered here the initial physical size of each aggregate is comparable to its Hill radius. Low-velocity impacts with $v_{\text{imp}}/v_{\text{esc}} \lesssim 0.5$ result in accretion, because deformation of the combined aggregate is small and all constituent particles settle inside the Hill sphere after the impact. However, when $v_{\text{imp}}/v_{\text{esc}} \gtrsim 0.5$, the combined aggregate becomes radially elongated after the impact and keeps changing its shape because of the tidal force and the shear motion, and eventually it is totally disrupted (Figure 9, left). With increasingly higher impact velocity, disruption is facilitated not only by the elongation of the aggregate shape but also by the fact that part of the constituent particles are gravitationally dispersed as a result of collisions (Figure 9, middle and right panels). Therefore, in the strong tidal field such as the radial location of the F ring, collision outcomes are completely different among radial, azimuthal, and vertical collisions.

4.2. Dependence on the Radial Distance from the Planet

So far, we have presented results in the case of the strong tidal effect, corresponding to the radial location of the F ring. Next, we examine the dependence of collision outcomes on the radial distance from the central planet. Figure 10 shows results of simulations of radial collisions for various radial locations. The plots are similar to the one shown in the top panel of Figure 5, but in the present case, those for six radial distances from Saturn are shown (150,000–200,000 km). In the case of

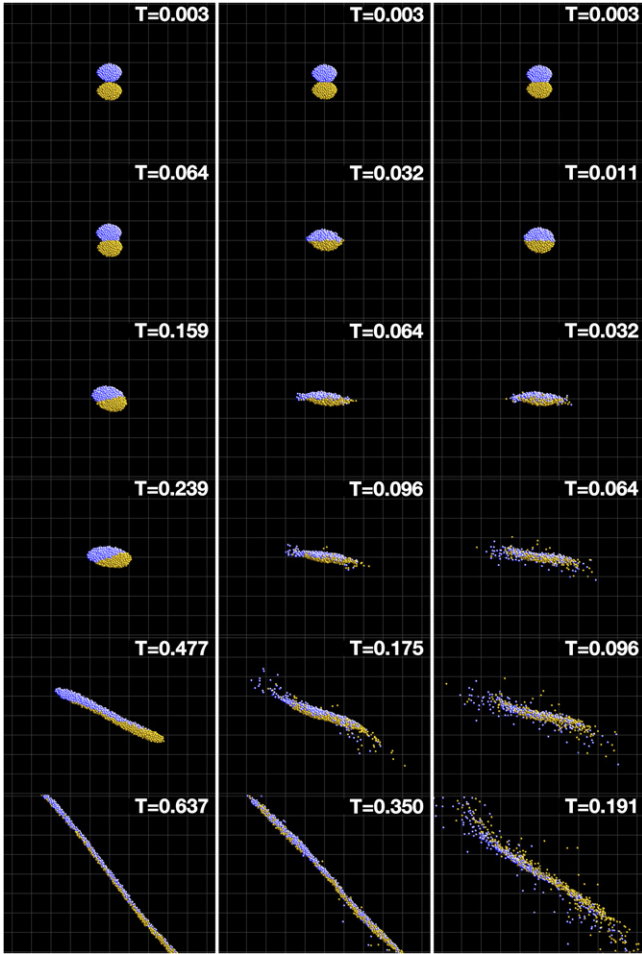


Figure 8. Same as Figure 6, but time series of simulations of collisions between aggregates in the azimuthal direction in the strong tidal environment ($a = 140,000$ km) are shown. Three cases with different impact velocities are shown: $v_{\text{imp}}/v_{\text{esc}} = 0.02$ (left), $v_{\text{imp}}/v_{\text{esc}} = 1.90$ (middle), and $v_{\text{imp}}/v_{\text{esc}} = 3.81$ (right).

(An animation and a color version of this figure are available in the online journal.)

$a = 150,000$ km (Figure 10(a)), the overall dependence on impact velocity is similar to the case of the F ring (Figure 5, top), but there are some differences. In the case of $a = 150,000$ km, the disruption efficiency in Region B is lower, and the mass fraction of the largest remnant is somewhat larger. Also, Region C becomes somewhat wider because the size of the Hill radius becomes larger with increasing radial distance. In the case of $a = 160,000$ km (Figure 10(b)), Region B disappears, and most of the low-velocity impacts with $v_{\text{imp}}/v_{\text{esc}} < 1$ now result in accretion, except for the very low-velocity case where colliding aggregates remain nearly intact. As a result, Region C becomes wider, while the disruption efficiency in Region D becomes lower. When the distance from the planet is further increased to 180,000 km (Figure 10(d)), Region A disappears and the disruption efficiency in Region D becomes significantly lower. This is because at this distance the value of \tilde{r}_p is 0.70; thus, the Hill sphere of the aggregate becomes larger than its physical size. When the radial distance becomes as large as $a = 190,000$ km, even Region D disappears, and when $a = 200,000$ km (Figure 10(f)), the overall behavior becomes similar to the case of collisions in free space, i.e., the mass fraction of the largest remnant becomes smaller with increasing impact velocity.

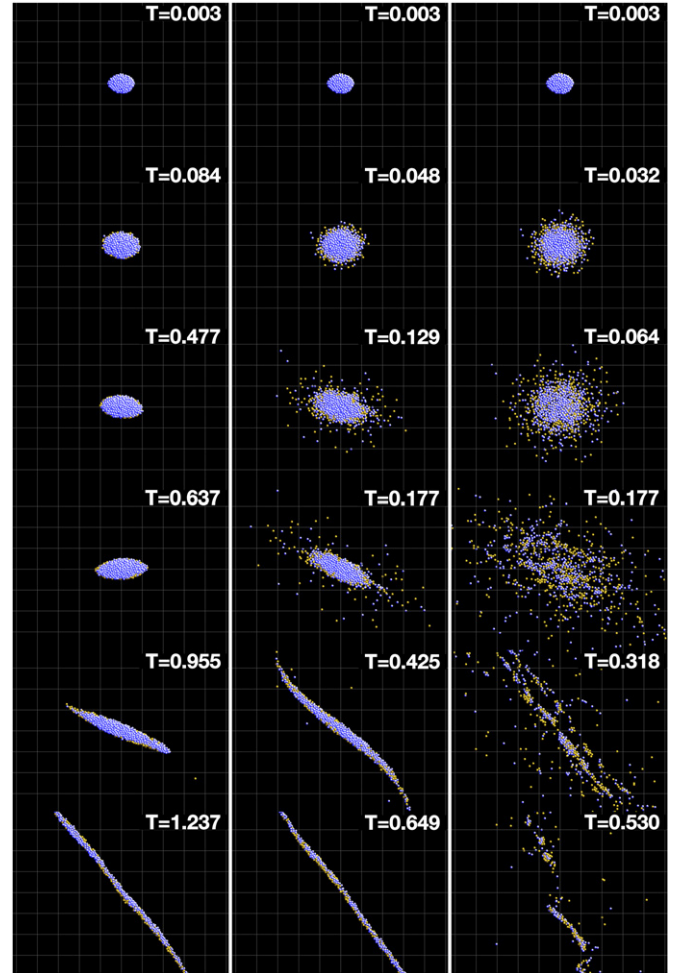


Figure 9. Same as Figure 6, but time series of simulations of collisions between aggregates in the vertical direction in the strong tidal environment ($a = 140,000$ km) are shown. Note that in the top panels the aggregate colored yellow is hidden under the blue one (see Figure 3, right panel). Three cases with different impact velocities are shown: $v_{\text{imp}}/v_{\text{esc}} = 0.72$ (left), $v_{\text{imp}}/v_{\text{esc}} = 1.90$ (middle), and $v_{\text{imp}}/v_{\text{esc}} = 3.81$ (right).

(A color version of this figure is available in the online journal.)

Figure 11 shows results of azimuthal collisions for various radial locations. As in the case of radial collisions, we find that the tendency of accretion in low-velocity impacts becomes more notable as the radial distance is increased. We find that azimuthal collisions tend to be significantly more disruptive than radial collisions when $a \leq 170,000$ km and $2 \lesssim v_{\text{imp}}/v_{\text{esc}} \lesssim 3$, because of the fact that the initial aggregate is elongated to the radial direction and also because of the Coriolis force in the radial direction at the time of impact, as mentioned in Section 4.1. However, with further increase in the radial distance ($a = 190,000$ km, Figure 11(e)), the mass fraction of the largest remnant becomes a rather smooth, monotonically decreasing function of impact velocity, similar to the case of collisions in free space (Stewart & Leinhardt 2009; Leinhardt & Stewart 2012). This can be explained by the fact that the Hill sphere of the aggregate becomes sufficiently larger than its physical size at this radial location since the value of \tilde{r}_p becomes 0.66, and the aggregate disruption occurs when particles have a sufficiently large velocity after the impact. On the other hand, we also note that azimuthal collisions are slightly more disruptive than radial collisions even at the location far outside the Roche limit ($a > 180,000$ km; see the difference at $v_{\text{imp}}/v_{\text{esc}} \simeq 3$). This

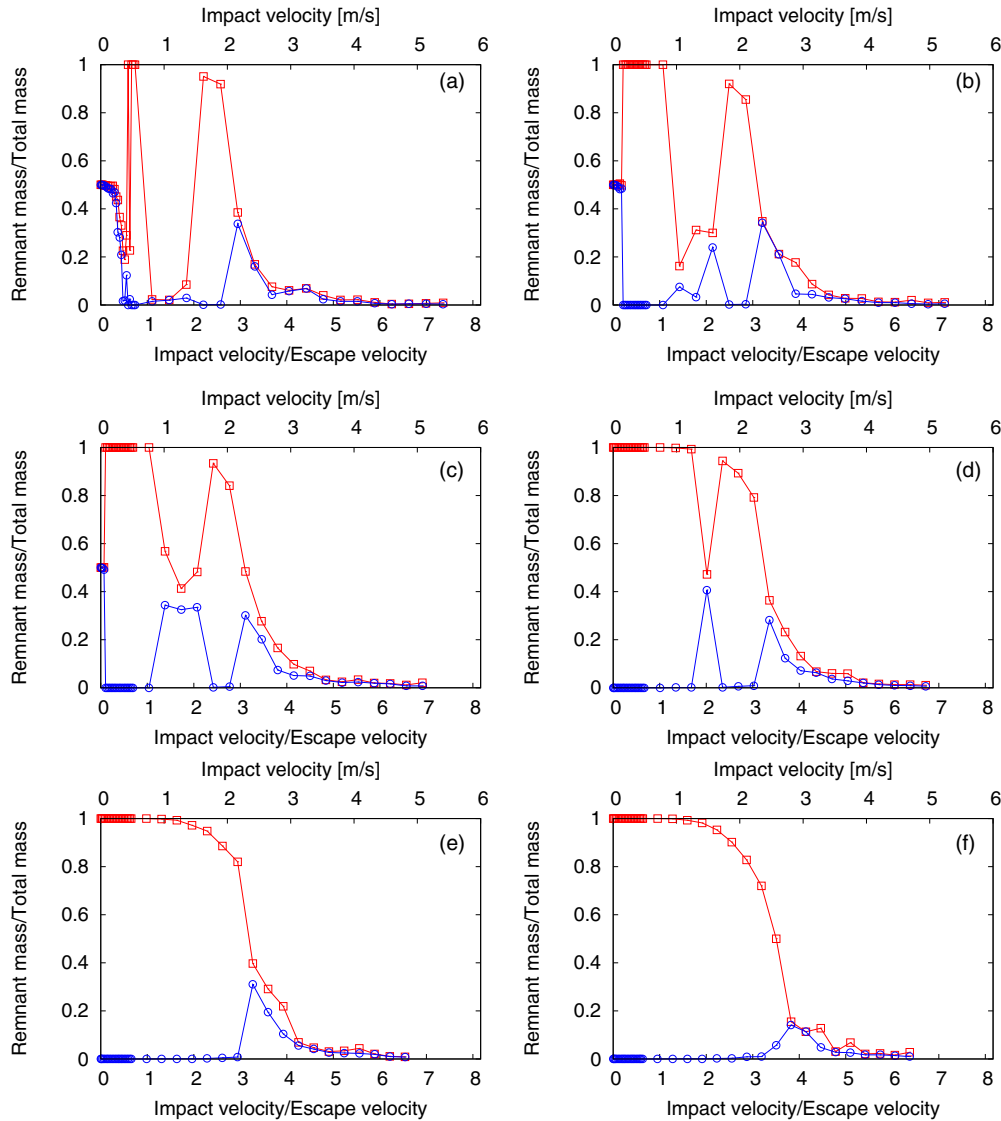


Figure 10. Same as the top panel of Figure 5, but results of simulations of radial collisions for various radial distances from Saturn are shown: (a) 150,000 km, (b) 160,000 km, (c) 170,000 km, (d) 180,000 km, (e) 190,000 km, and (f) 200,000 km.

(A color version of this figure is available in the online journal.)

is because in the case of azimuthal collisions between such elongated aggregates, more particles tend to be dispersed in the radial direction at the time of collision than in the case of radial collisions. Then, these particles are further dispersed because of the shear motion in the azimuthal direction. Thus, gravitational reaccumulation becomes more difficult in the case of azimuthal collisions. Figure 12 shows similar plots for vertical collisions. As in the case of radial and azimuthal collisions, with increasing radial distance from Saturn, accretion becomes notable in low-velocity impacts and the transition from total accretion to total disruption becomes smoother.

In summary, in the case of a strong tidal field, tidal deformation of aggregates plays an essential role in collisional disruption. In this case, because the Hill sphere of the aggregate is comparable to its physical size, even small elongation of the aggregate to the radial direction can lead to complete disruption. On the other hand, the ratio of the Hill radius to the physical size increases with increasing distance from the central planet. When the ratio is sufficiently large, collision outcome is determined by the post-impact velocity of constituent particles; accretion

occurs when impact velocity is sufficiently small. The results for $a = 200,000$ km in Figures 10–12 suggest that the effect of the tidal force is relatively weak in this case. In such a case, the mass fraction of the largest remnant is a monotonically decreasing function of impact velocity, as in the case of collisions in free space.

In all the simulations presented above, we have used initial aggregates of the same shape to eliminate the influence of aggregate shape, as mentioned before. However, aggregates formed by gravitational accretion are expected to become rounder with increasing radial distance from the planet (Karjalainen & Salo 2004; Karjalainen 2007). In order to examine the degree of the influence of aggregate shape in our simulation results, especially in the case of weak tidal force where aggregates are expected to take a nearly spherical shape, we performed additional simulations of impacts between spherical aggregates at $a = 200,000$ km (Figure 13). In the relatively low-velocity regime with $v_{\text{imp}}/v_{\text{esc}} \lesssim 1$, collisions lead to accretion regardless of the direction of impact (radial, azimuthal, or vertical) or initial shape (ellipsoid or sphere) of the aggregates. In the case

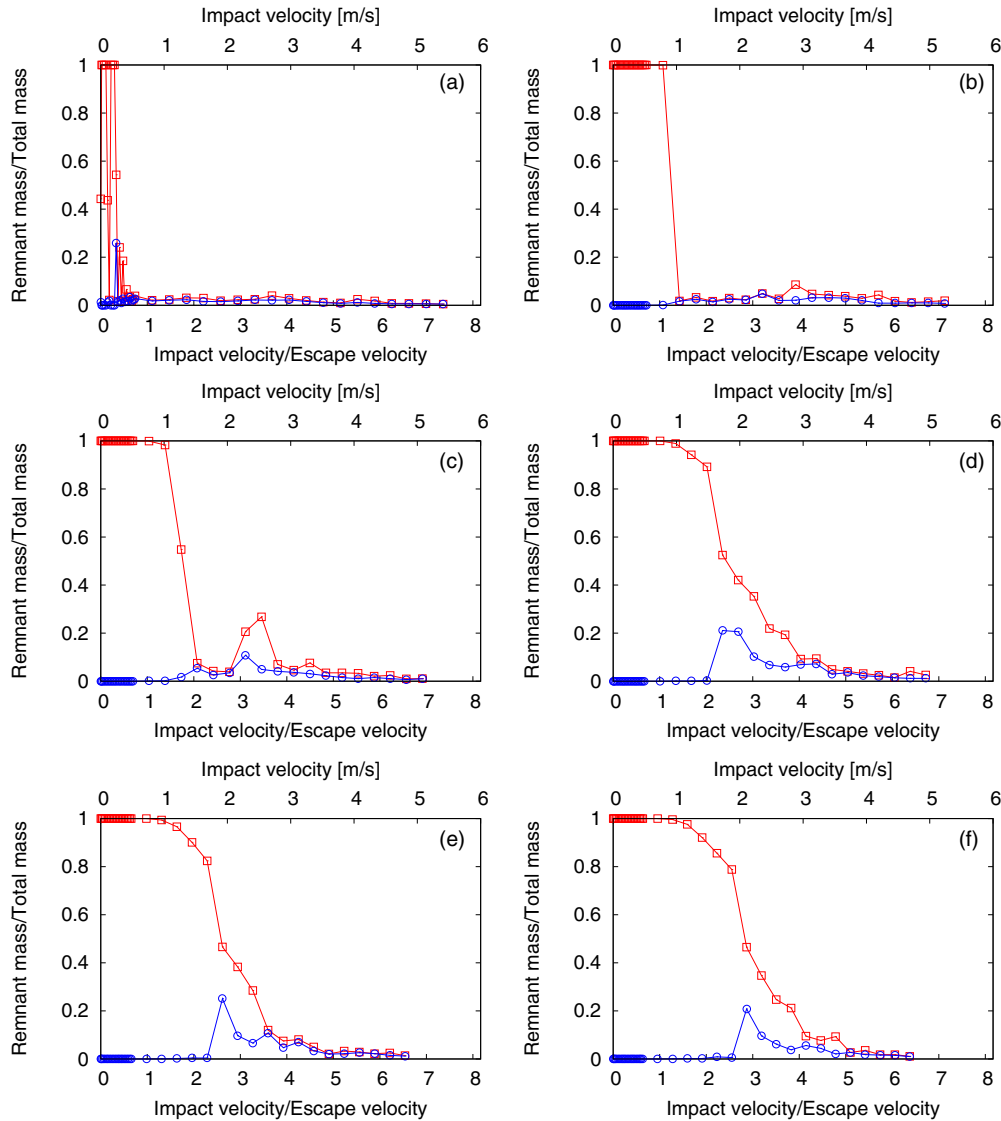


Figure 11. Same as the middle panel of Figure 5, but results of simulations of azimuthal collisions for various radial distances from Saturn are shown: (a) 150,000 km, (b) 160,000 km, (c) 170,000 km, (d) 180,000 km, (e) 190,000 km, and (f) 200,000 km. (A color version of this figure is available in the online journal.)

of higher velocities with $2 \lesssim v_{\text{imp}}/v_{\text{esc}} \lesssim 5$, on the other hand, there are significant differences among the six cases. When we compare the results of radial, azimuthal, and vertical collisions in either the case of ellipsoidal aggregates or in the spherical case in Figure 13, we confirm that azimuthal collision is the most destructive and the radial collision is the least destructive (see also Figures 5, 10, 11, and 12). This is because more particles tend to become gravitationally dispersed and gravitational reaccumulation is the least efficient because of the shear motion in azimuthal collisions. On the other hand, comparing the results for ellipsoidal aggregates with those of spherical aggregates in Figure 13, the ellipsoidal aggregates are more easily disrupted than the spherical ones at radial collision, while the spherical ones are more easily disrupted in the case of azimuthal collision. We think that this can be explained by the difference in the efficiency of energy transfer at the time of impact due to different radii of curvature at the points of contact between the colliding aggregates. That is, when two ellipsoidal aggregates collide in the radial direction, the area of contact at the time of impact is smaller compared with the case of spherical aggregates of the

same total mass. Thus, impact energy is more localized near the point of impact and can be used for disruption more efficiently, resulting in a smaller mass fraction of the largest remnant. On the other hand, when the ellipsoidal aggregates collide in the azimuthal direction, the area of contact at the time of impact becomes larger compared with the case of spherical aggregates; thus, the collision becomes less disruptive than the azimuthal collision between spherical aggregates. A similar explanation can be made for the difference between spherical and ellipsoidal aggregates in vertical collisions. However, the general tendency of the mass fraction of the largest remnant to become smaller with increasing impact velocity is the same for the six cases.

4.3. Dependence on the Restitution Coefficient

In the simulations presented so far, we set the normal coefficient of restitution ε_n to be 0.25. However, the physical properties of ring particles are largely unknown. Laboratory experiments for ice show that ε_n depends on impact velocity and is close to unity for impacts with sufficiently low velocities

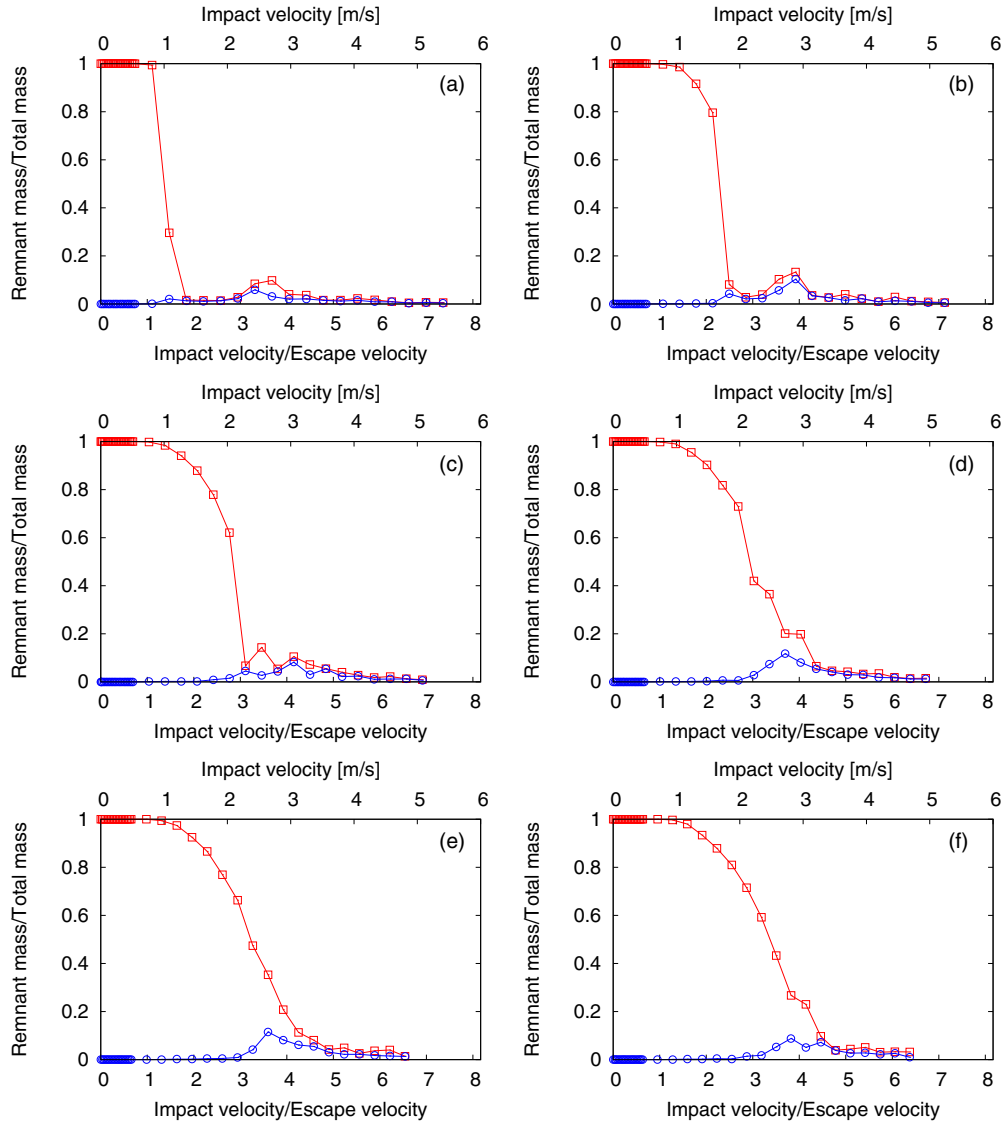


Figure 12. Same as the bottom panel of Figure 5, but results of simulations of vertical collisions for various radial distances from Saturn are shown: (a) 150,000 km, (b) 160,000 km, (c) 170,000 km, (d) 180,000 km, (e) 190,000 km, and (f) 200,000 km.

(A color version of this figure is available in the online journal.)

(e.g., Bridges et al. 1984; Hatzes et al. 1988). In order to investigate the dependence of collision outcomes on the coefficient of restitution, we performed simulations of radial collisions with $\varepsilon_n = 0.75$ for $a = 140,000$ km and $200,000$ km. The left panel of Figure 14 shows the results for $a = 140,000$ km with $\varepsilon_n = 0.25$ and 0.75 . In the region with low impact velocities corresponding to Regions A and B in the left panel of Figure 5, the results with two different values of ε_n are very similar. In this case, collision outcomes are regulated by the deformation of colliding aggregates as we mentioned in Section 4.1, which is rather insensitive to the assumed values of ε_n . In contrast, the behavior in the high-velocity regime with $v_{\text{imp}}/v_{\text{esc}} \gtrsim 1$ is different when ε_n is increased. The high-velocity regime corresponding to Region E in the left panel of Figure 5 shifts toward the lower velocity region in the case of a higher restitution coefficient. In the high-velocity regime corresponding to Region E, collisions with a higher coefficient of restitution tend to be more disruptive, because particles can have larger velocity after impact and can more easily escape from the gravity of the aggregates. The right panel of Figure 14 shows the results for $a = 200,000$ km,

where we can see a tendency similar to that of the high-velocity regime in the left panel of Figure 14. These results suggest that elastic properties of constituent particles are important in the regime where collision outcomes are determined by ejection velocity of the particles, while collision outcomes are rather insensitive to the elastic properties for low-velocity collisions in the strong tidal effect, where post-impact deformation plays a major role.

5. CRITERIA FOR CATASTROPHIC DISRUPTION

The degree of collisional disruption is often expressed by using the ratio of the mass of the largest remnant (m_r) to the total mass (m_{tot}) of an impactor and a target as we described above, and in the case of collisions in free space, m_r/m_{tot} is a monotonically decreasing function of the specific impact energy. The specific impact energy defined in terms of the masses of the impactor and the target as $Q = (1/2)m_{\text{impactor}}v_{\text{imp}}^2/m_{\text{target}}$ was usually used in previous works implicitly assuming $m_{\text{impactor}} \ll m_{\text{target}}$, but Stewart & Leinhardt (2009) used an expression of

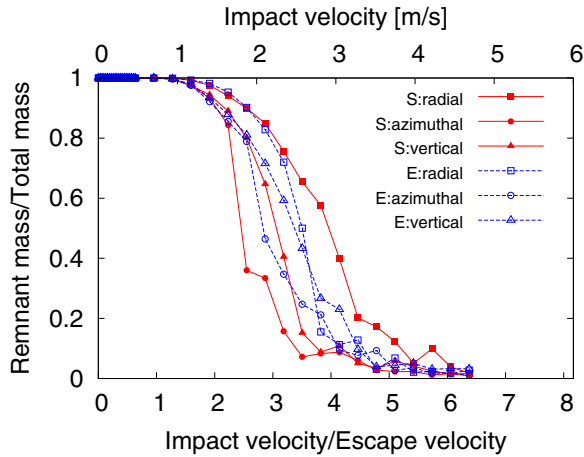


Figure 13. Numerical results of radial, azimuthal, and vertical collisions at $a = 200,000$ km using two different shapes of aggregates. Radial, azimuthal, and vertical collisions using spherical aggregates (denoted by “S”) are plotted by the filled red marks with solid lines (squares, circles, and triangles, respectively). Radial, azimuthal, and vertical collisions using ellipsoidal aggregates (denoted by “E”) are plotted by the open blue marks with dashed lines (squares, circles, and triangles, respectively).

(A color version of this figure is available in the online journal.)

the impact energy defined by $Q_R = (1/2)\mu v_{\text{imp}}^2/m_{\text{tot}}$, where $\mu = m_{\text{target}}m_{\text{impactor}}/m_{\text{tot}}$ is the reduced mass (see also Takeda & Ohtsuki 2007). Stewart & Leinhardt (2009) showed that outcomes of collisions with various impactor-to-target mass ratios can be understood in a unified manner if Q_R is used (see also Leinhardt & Stewart 2012). They derived a universal law for the largest remnant given by

$$m_{\text{lr}}/m_{\text{tot}} = -0.5(Q_R/Q_{\text{RD}}^* - 1) + 0.5 \quad (10)$$

for $0 < Q_R/Q_{\text{RD}}^* < 2$, where Q_{RD}^* is the value of Q_R required to gravitationally disperse half the total mass.

As we mentioned in Section 3, we performed simulations of head-on collisions in free space as a test of our simulation code. Figure 15 shows the mass fraction of the largest remnant as a function of the normalized specific impact energy in this case. We find that our numerical results are consistent with the result of Leinhardt & Stewart (2012); mass fraction of the largest remnant is a monotonically decreasing function of the specific impact energy and can be approximated by Equation (10).

Next, we examine the validity of the above universal law in the case of collisions in the tidal environment. Figure 16

shows the mass fraction of the largest remnant as a function of the normalized specific impact energy at four different radial distances from Saturn. Here Q_{RD}^* is calculated by fitting the results of radial collisions between spherical aggregates in the case of $a = 200,000$ km. We show results of the ellipsoidal aggregates and those with spherical ones in the case of $a = 200,000$ km (Figure 16(d)) as in Figure 13, while the results for the ellipsoidal aggregates are shown in the other cases. The results of radial collisions between spherical aggregates at $a = 200,000$ km agree well with the linear relationship given above, demonstrating the validity of the universal law in such a case. At this radial location, the Hill radius of the aggregate is sufficiently larger than its physical size. Also, radial impacts tend to disperse particles mainly in the azimuthal direction, and the tidal effect on particle dispersal is weaker and thus reaccumulation is more efficient compared with the case of azimuthal and vertical collisions, as we mentioned before. These factors seem to explain the above rather good agreement with the linear relationship. In the case of low-velocity collisions corresponding to $0 < Q_R/Q_{\text{RD}}^* < 0.5$ in Figure 16(d), numerical results are plotted near the line for the universal law, regardless of the initial shape of the aggregates and the direction of the collision. However, at higher impact velocities, even at the same radial distance ($a = 200,000$ km), results of the five cases other than the radial collisions for spherical aggregates largely deviate from the universal law (see also Figure 13). The deviation is more significant for the cases with the stronger tidal effects (Figures 16(a)–(c)), which can be expected from the results shown above (e.g., Figures 5, 10, 11, and 12). As we mentioned in Section 3, even though the velocities of the colliding aggregates are initially given so that they are pointing toward the center of the other, aggregate centers slightly curve away from each other in the case of radial and azimuthal collisions because of the Coriolis force before the aggregates overlap significantly. Thus, strictly speaking, aggregates in the case of radial and azimuthal collisions experience oblique impacts in our simulation frame, and the impact parameter is correlated with the impact velocity (see Equation (9)). However, this is not the reason for the above deviation from the universal law, because Leinhardt & Stewart (2012) shows that oblique impacts in free space can be well approximated by the universal law (their Figure 3). On the other hand, in the case of vertical collisions, the aggregates experience exactly head-on collisions in our chosen frame, but still the results in the strong tidal environment shown in Figure 16 largely deviate from the universal law. Therefore, we can conclude that

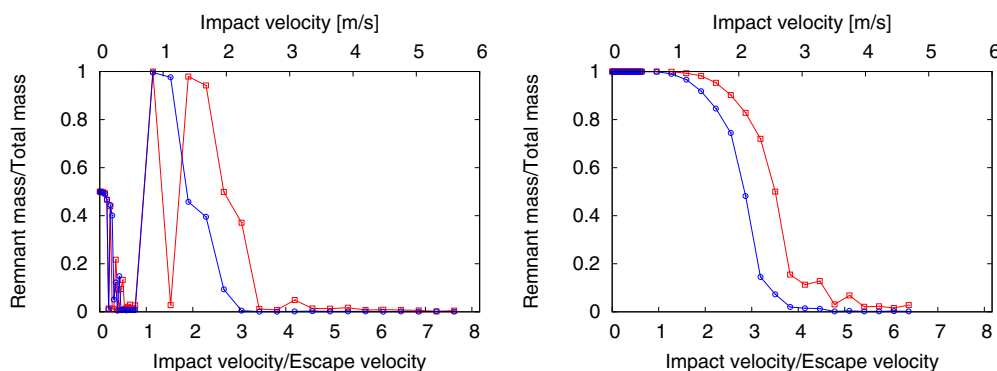


Figure 14. Numerical results of radial collisions using two different values of coefficient of restitution: $\epsilon_n = 0.25$ (red line with squares) and $\epsilon_n = 0.75$ (blue line with circles). The left panel shows the results for $a = 140,000$ km, and the right panel shows the case of $a = 200,000$ km.

(A color version of this figure is available in the online journal.)

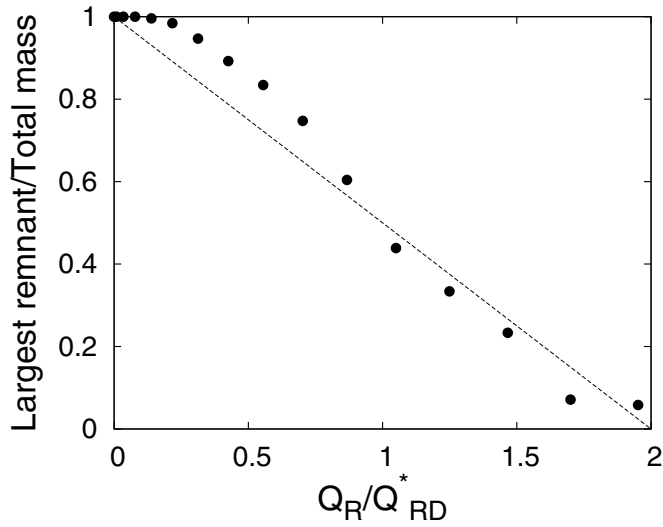


Figure 15. Mass fraction of the largest remnant as a function of the normalized specific impact energy for the case of head-on collisions in free space. The filled circles are results of our simulation (mass ratio is 1:1), while the analytic linear relationship given by Equation (10) is shown by the dashed line.

the universal law seems to be valid when the radial distance from the planet is large enough to neglect the tidal effects, but it cannot be directly applied to collisions at locations where the tidal effect is important.

6. SUMMARY

In the present work, we investigated collisions between gravitational aggregates in the tidal environment, which is important for the origin and dynamical evolution of ring-satellite systems of giant planets. Outcomes of collisions under the tidal effect largely depend on the magnitudes of the radial, azimuthal, and vertical components of impact velocity, which vary significantly depending on the random velocity, the difference in semimajor axes, and the orbital phase angles of colliding bodies (Section 2.2). We performed local N -body simulations of aggregate impacts including the tidal force, and we examined the dependence of collision outcomes on various parameters, such as the impact velocity, the direction of the collision, and the distance from the central planet. In the case for a strong tidal field such as Saturn's F ring, we found that outcomes of collisions largely depend on the direction of impact, i.e., a collision in the azimuthal direction is the most destructive because of the Coriolis force and the tidal force, while a radial collision is the least destructive. In the case of radial collisions in such a strong tidal field, we found that collision outcomes sensitively depend on the impact velocity. Tidal deformation of colliding aggregates after the impact plays an essential role in low-velocity collisions, while the velocity of dispersed particles after the impact determines the degree of disruption in high-velocity collisions and the mass of the largest remnant aggregate becomes smaller with increasing impact velocity. Numerical results are insensitive to the value of the restitution coefficient in the former low-velocity case, while higher values of the coefficient facilitate disruption

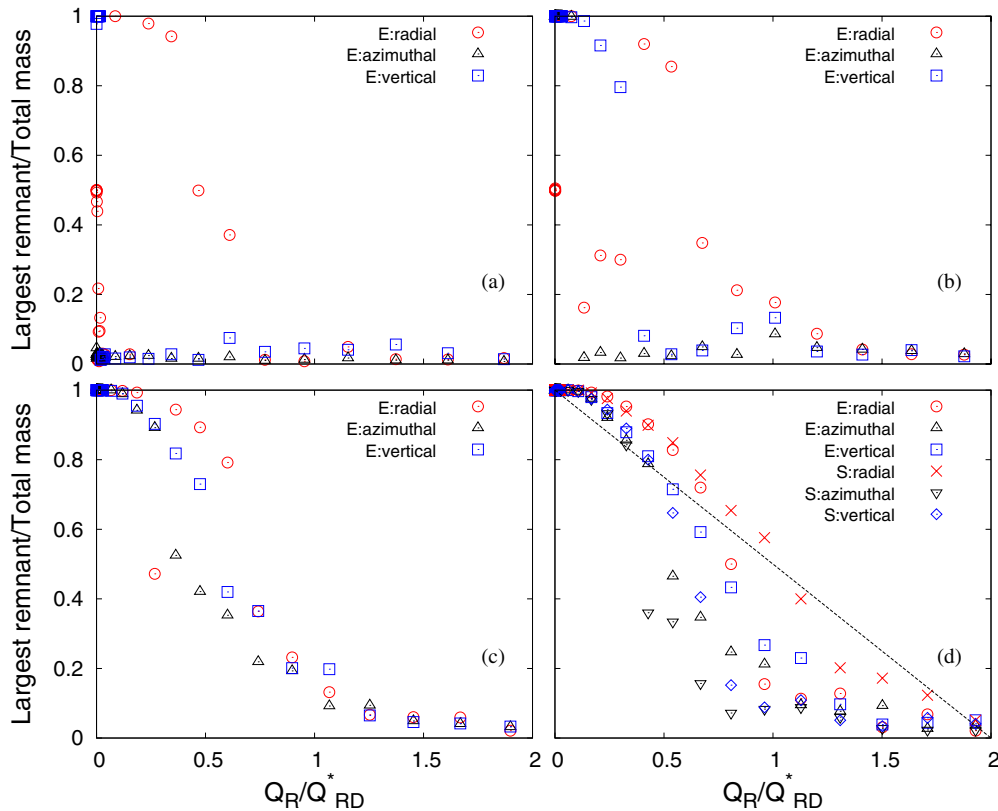


Figure 16. Mass fraction of the largest remnant as a function of the normalized specific impact energy. Numerical results for four different radial distances are shown: (a) 140,000 km, (b) 160,000 km, (c) 180,000 km, and (d) 200,000 km from Saturn. Results for radial, azimuthal, and vertical collisions between elongated aggregates are shown by red circles, black triangles, and blue squares, respectively. In panel (d), results for radial, azimuthal, and vertical impacts between spherical aggregates (red crosses, black reversed triangles, and blue diamonds, respectively) as well as the analytic linear relationship given by Equation (10) (dashed line) are also shown. (A color version of this figure is available in the online journal.)

in the latter high-velocity case. We also examined the dependence of collision outcomes on the radial distance from the planet. We found that at radial locations sufficiently far from the planet (where $\tilde{r}_p \lesssim 0.7$ for a pair of colliding constituent particles; $a \gtrsim 180,000$ km in the case of the Saturnian system), the mass of the largest remnant becomes a monotonically decreasing function of impact velocity, as in collisions in free space. However, we also noticed that the tidal effect is significant even at $a = 200,000$ km in the case of the Saturnian system, especially in collisions in the azimuthal direction. Stewart & Leinhardt (2009) derived an analytic linear relationship between the mass fraction of the largest remnant and the normalized specific impact energy, which they called the universal law. We examined its validity in the case of aggregate impacts in the tidal environment. We found that outcomes of radial collisions seem to agree well with the universal law when the radial distance is large enough. However, even at $a = 200,000$ km from Saturn, the tidal effect is found to be significant, especially for azimuthal collisions.

The results of the present work show that in the strong tidal field such as the F ring, both accretion and disruption take place in collisions between gravitational aggregates. This is consistent with the *Cassini* observations that suggest the occurrence of both particle accretion and collisional disruption in the F ring (Beurle et al. 2010; Attree et al. 2012). These observations revealed detailed structures likely caused by gravitational accretion or disruption of aggregates, and they also show the time variation of such structures. Comparison between these observations and numerical simulations of such processes would provide new insights, such as the detailed mechanism of the creation of such structures and/or constraints on physical properties of ring particles. We plan to work on such issues in our subsequent work.

We thank Nicole Albers, Larry Esposito, Derek Richardson, Glen Stewart, and Eiichiro Kokubo for discussion. We also thank the anonymous reviewer for comments that improved the presentation of the manuscript. This work was supported by JSPS KAKENHI and by NASA's Planetary Geology and Geophysics Program. Part of the numerical simulations were performed using the computer systems at the National Astronomical

Observatory of Japan. The article charges for this paper were partly supported by the Center for Computational Astrophysics, National Astronomical Observatory of Japan.

REFERENCES

- Attree, N. O., Murray, C. D., Cooper, N. J., & Williams, G. A. 2012, *ApJL*, **755**, L27
- Barbara, J. M., & Esposito, L. W. 2002, *Icar*, **160**, 161
- Beurle, K., Murray, C. D., Williams, G. A., et al. 2010, *ApJL*, **718**, L176
- Bridges, F. G., Hatzes, A., & Lin, D. N. C. 1984, *Natur*, **309**, 333
- Canup, R. M., & Esposito, L. W. 1995, *Icar*, **113**, 331
- Chandrasekhar, S. 1969, *Ellipsoidal Figures of Equilibrium* (New Haven, CT: Yale Univ. Press)
- Charnoz, S., Salmon, J., & Crida, A. 2010, *Natur*, **465**, 752
- Crida, A., & Charnoz, S. 2012, *Sci*, **338**, 1196
- Hatzes, A. P., Bridges, F., & Lin, D. N. C. 1988, *MNRAS*, **231**, 1091
- Karjalainen, R. 2007, *Icar*, **189**, 523
- Karjalainen, R., & Salo, H. 2004, *Icar*, **172**, 328
- Leinhardt, Z. M., Ogilvie, G. I., Latter, H. N., & Kokubo, E. 2012, *MNRAS*, **424**, 1419
- Leinhardt, Z. M., & Richardson, D. C. 2002, *Icar*, **159**, 306
- Leinhardt, Z. M., Richardson, D. C., & Quinn, T. 2000, *Icar*, **146**, 133
- Leinhardt, Z. M., & Stewart, S. T. 2012, *ApJ*, **745**, 79
- Nakazawa, K., Ida, S., & Nakagawa, Y. 1989, *A&A*, **220**, 293
- Ohtsuki, K. 1993, *Icar*, **106**, 228
- Ohtsuki, K. 2012, *PThPS*, **195**, 29
- Ohtsuki, K., Yasui, Y., & Daisaka, H. 2013, *AJ*, **146**, 25
- Porco, C. C., Thomas, P. C., Weiss, J. W., & Richardson, D. C. 2007, *Sci*, **318**, 602
- Quinn, T., Perrine, R. P., Richardson, D. C., & Barnes, R. 2010, *AJ*, **139**, 803
- Roche, R. A. 1847, *Acad. des Sciences et Lettres de Montpellier, Mem. de la Section des Sciences*, **1**, 243
- Schmidt, J., Ohtsuki, K., Rappaport, N., Salo, H., & Spahn, F. 2009, in *Saturn from Cassini-Huygens*, ed. M. K. Dougherty et al. (New York: Springer), **413**
- Showalter, M. R. 1998, *Sci*, **282**, 1099
- Stewart, S. T., & Leinhardt, Z. M. 2009, *ApJL*, **691**, L133
- Takeda, T., & Ohtsuki, K. 2007, *Icar*, **189**, 256
- Takeda, T., & Ohtsuki, K. 2009, *Icar*, **202**, 514
- Tiscareno, M. S., Hedman, M. M., Burns, J. A., & Castillo-Rogez, J. 2013, *ApJL*, **762**, L28
- Walsh, K. J., & Richardson, D. C. 2003, *BAAS*, **35**, 1486
- Weidenschilling, S. J., Chapman, C. R., Davis, D. R., & Greenberg, R. 1984, in *Planetary Rings*, ed. R. Greenberg & A. Brahic (Tucson, AZ: Univ. Arizona Press), **367**